

to be submitted to The Astrophysical Journal

**Carbon abundance in Small Magellanic Cloud planetary nebulae  
through *Advanced Camera for Surveys* prism spectroscopy:  
constraining stellar evolution at low metallicity.**

Letizia Stanghellini

*National Optical Astronomy Observatory, 950 N. Cherry Av., Tucson, AZ 85719*

lstanghellini@noao.edu

Ting-Hui Lee

*Department of Physics and Astronomy, Western Kentucky University, 1906 College  
Heights Blvd #11077, Bowling Green, KY 42101*

ting-hui.lee@wku.edu

Richard A. Shaw

*National Optical Astronomy Observatory, 950 N. Cherry Av., Tucson, AZ 85719*

shaw@noao.edu

Bruce Balick

*Astronomy Department, Box 351580, University of Washington, Seattle WA 98195*

balick@astro.washington.edu

and

Eva Villaver

*Universidad Autónoma de Madrid, Departamento de Física Teórica C-XI, 28049 Madrid,  
Spain*

eva.villaver@uam.es

**ABSTRACT**

We perform near ultraviolet ACS prism spectroscopy of 11 Small Magellanic Cloud (SMC) planetary nebulae (PNe) with the main aim of deriving the abundance of carbon. The analysis of the ACS spectra provide reliable atomic carbon abundances for all but a couple of our targets; ionic  $C^{2+}$  abundances are calculated for all target PNe. With the present paper we more than double the number of SMC PNe with known carbon abundances, providing a good database to study the elemental evolution in low- and intermediate-mass stars at low metallicity. We study carbon abundances of Magellanic Cloud PNe in the framework of stellar evolution models and the elemental yields. Constraining SMC and LMC stellar evolutionary models is now possible with the present data, through the comparison of the final yields calculated and the CNO abundances observed. We found that SMC PNe are almost exclusively carbon rich, and that for the most part they have not undergone the hot-bottom burning phase, contrary to  $\sim$ half of the studied LMC PNe. The yields from stellar evolutionary models with LMC and SMC metallicities broadly agree with the observations. In particular, evolutionary yields for  $M_{\text{to}} < 3.5 M_{\odot}$  well encompass the abundances of round and elliptical PNe in the SMC. We found that the carbon emission lines are major coolants for SMC PNe, more so than in their LMC counterparts, indicating that metallicity has an effect on the physics of PNe, as predicted by Stanghellini et al. (2003).

*Subject headings:* Planetary nebulae, stellar evolution, nucleosynthesis, ultraviolet spectroscopy, Magellanic Clouds

## 1. Introduction

Planetary Nebulae (PNe) have been studied for decades, and through those efforts an understanding has come of the final phases of stellar evolution of stars with masses in the  $\sim 1 - 8 M_{\odot}$  range (also called the low- and intermediate-mass stars, or LIMS). Planetary nebulae are ejected toward the end of the LIMS evolution, during the final thermal pulses on the Asymptotic Giant Branch (TP-AGB), thus they are ideal probes to test the ISM enrichment from these stars in a quantitative way. The scientific importance of studying PNe in the Magellanic Clouds (LMC, SMC) can be very simply summarized: LMC and SMC PNe are absolute probes of stellar and nebular brightness, size, and shape, because their distance is relatively well known, and because their interstellar extinction is comparatively low and uniform. In particular, the SMC is a unique laboratory to study resolved stellar populations in a low metallicity environment: chemical analysis of the PNe therein gives a direct test

of cosmic recycling at low metallicity, which is essential to understanding the recycling of elements within galaxies at high redshift.

The gas ejected at the PN phase contains elements that have been produced in the stellar interiors, and then carried to the stellar surface by the convective dredge-up processes (Iben & Renzini 1983, van den Hoek & Groenewegen 1997). The single-star evolution models predict a chemical enrichment of the outer region of evolved LIMS, both for Galactic and Magellanic Cloud LIMS alike, which can be summarized as follows:

During the first Red Giant phase, the convective envelope penetrates regions that are partially CNO-processed. This dredge-up results in a  $^{13}\text{C}$  and  $^{14}\text{N}$  enhancement, and a decrease of  $^{12}\text{C}$ . Afterward, He-burning starts in the stellar core. Later, the hydrogen and helium burning occur alternately in two nuclear burning shells, surrounding the CO core, and the star ramps up to the AGB.

The second convective dredge-up (for  $M_{\text{to}}$ , the *turnoff* mass, larger than  $\sim 3 M_{\odot}$ ) occurs at the onset of the AGB phase, when the H-burning shell is temporarily extinguished. This process carries  $^4\text{He}$ ,  $^{13}\text{C}$ , and  $^{14}\text{N}$ -rich material to the stellar surface.

During the TP-AGB phase, the envelope is able to dredge-up material after each thermal pulse, carrying  $^4\text{He}$ ,  $^{12}\text{C}$ , and other relatively light s-process elements to the surface. This process is called the third dredge-up.

For  $M_{\text{to}} > 3\text{--}5 M_{\odot}$  (exact mass depends on metallicity, Marigo 2001), an additional process is thought to occur that alters the chemical composition: the so-called hot-bottom burning (HBB) that processes most of the carbon into nitrogen, occurring during the quiescent interpulse periods between thermal pulses.

The key to assessing the above predictions is to measure the abundances of the processed elements, particularly C, N, and O. Carbon and nitrogen enrichment depends on the progenitor mass, yielding to a direct connection between observed progenitor mass (i. e., population) and chemical content. By measuring the C and N abundances in PNe, one can at once validate key elements of stellar evolution theory, and measure the contribution of LIMS to the enrichment of the ISM. While O and N abundance analysis is straightforward to do with PNe, owing to their bright optical emission lines, the carbon analysis requires satellite UV spectroscopy.

In our earlier study of LMC PN abundances (Stanghellini et al. 2005) we have shown that PN morphology is a surprisingly useful indicator of the progenitor stellar evolution

and population. We used a subsample of LMC PNe images available from *HST*<sup>1</sup> and measured the carbon abundances with STIS spectroscopic analysis. We found that nitrogen enhancement is correlated with asymmetry. These results are consistent with the predictions of stellar evolution only if the progenitors of asymmetric PNe have on average larger masses than the progenitors of symmetric PNe. Our results are the first of the kind for extra-galactic PNe, and are thus not biased by the large selection effects that limit the observation of PNe in the Galactic disk.

Owing to the smaller metal abundance in the SMC than in the LMC, it is very important to extend the LMC study to the SMC. Carbon abundance determination in SMC PNe would probe the metal enrichment rates for low metallicity stellar population.

On these grounds we obtained near UV spectra of 11 SMC PNe that, together with the already published LMC and SMC UV data, provide a database that has a statistical impact on the study of carbon in Magellanic Cloud PNe. In the present paper we discuss the data acquisition and analysis of the ACS prism spectra (§2), the abundance analysis to derive carbon in SMC PNe (§3), and a discussion of our results in the framework on PN evolution and populations (§4). The conclusions are given in §5.

## 2. Observations and Data Analysis

### 2.1. Observations

We observed 11 SMC PNe using the Advanced Camera for Surveys (ACS) prisms PR130L in the Solar Blind Channel (SBC) and PR200L in the High Resolution Channel (HRC). Our aim is to detect the C IV  $\lambda 1550$ , the C III]  $\lambda 1909$ , and the C II]  $\lambda 2326$  nebular emission lines, to determine the ionic abundances of the carbon ions that are excited in the PN regime.

We select our targets from the SMC PNe that have been previously observed by us with the *Space Telescope Imaging Spectrograph* (STIS, Stanghellini et al. 2003; Shaw et al. 2006). With this selection we guarantee that their morphology, size, optical extinction, and optical fluxes are known. From the Stanghellini et al. (2003); Shaw et al. (2006) sample we chose all PNe that we deemed bright enough to be observed with the observing configuration within a few orbits (total  $H\beta$  fluxes larger than  $2.5 \times 10^{-14}$  [erg cm<sup>-2</sup> s<sup>-1</sup>]). In addition, our selected targets have angular sizes smaller than  $\lesssim 0.5''$  in order to prevent blending of emission lines

---

<sup>1</sup>LMC and SMC PNe are typically less than 0.5 arcsec across, they can be physically resolved from space.

in the slitless spectroscopy. The targets are listed in Table 1, together with the observing log. Of these, a few have been observed before with the IUE, but none has a sound carbon abundance determination.

The SBC detector is a  $1024 \times 1024$  solar-blind CsI Multi-Anode Microchannel Array (MAMA), with  $\sim 0.034 \times 0.030''$  pixels, and a nominal  $35 \times 31''$  field of view. The HRC detector is a  $1024 \times 1024$  SITe CCD with  $\sim 0.028 \times 0.025''$  pixels, covering a nominal  $29 \times 26''$  field of view. The wavelength range of SBC/PR130L is  $\sim 1200$ -  $2000 \text{ \AA}$ , and the useful wavelength range of HRC/PR200L is  $\sim 1800$ -  $4000 \text{ \AA}$ . The wavelength scale of the prisms is non-linear, with spectral resolution decreasing towards longer wavelengths. For PR130L, the dispersion varies from about  $2 \text{ \AA/pixel}$  at the blue end ( $R \sim 300$ ), to  $\sim 10 \text{ \AA/pixel}$  at  $1600 \text{ \AA}$  ( $R \sim 80$ ) and  $30 \text{ \AA/pixel}$  at the red end ( $R \sim 30$  at  $2000 \text{ \AA}$ ). For PR200L, the dispersion varies from about  $6 \text{ \AA/pixel}$  at the blue end ( $R \sim 150$ ), to  $\sim 20 \text{ \AA/pixel}$  at  $2500 \text{ \AA}$  ( $R \sim 60$ ) and  $\sim 200 \text{ \AA/pixel}$  at  $4000 \text{ \AA}$  ( $R \sim 10$ ) (Larsen et al. 2006; Larsen 2006).

For each target, the HRC observations consist of a direct image through a broad band filter (F330W), and two exposures through the prism (PR200L) in order to perform rejection of cosmic rays. Similarly, the SBC observations consist of a direct image through F165LP, and one exposure of PR130L, unless the exposure time is longer than one orbit, in which case two exposures were taken. The direct images have been acquired to establish the zero-point of the wavelength scale.

## 2.2. Data Analysis

The pipeline calibration of our data provided bias-subtracted, dark-corrected, and flat-corrected spectral images, as processed with CALACS (Pavlovsky et al. 2004). We used MultiDrizzle and aXe to combine the images, correct for geometric distortion, and to identify any bad pixels in the spectrum. The bad pixels were excluded from the analysis of our flux-calibrated one-dimensional spectra.

The position, size, and magnitude of the extracting sources were identified and determined using the direct images SBC/F165LP and HRC/F330W via analysis with SExtractor (Bertin & Arnouts 1996). The position of the extracting sources on the direct images have then been projected on the prism images for spectral extraction.

The spectral extraction was done with the aXe software (Kümmel et al. 2005) in PyRAF<sup>2</sup>. For prism slitless spectroscopy, the trace and wavelength solutions include spatial variations

---

<sup>2</sup>PyRAF is a product of the Space Telescope Science Institute, which is operated by AURA for NASA.

across the HRC and SBC detectors. The wavelength and flux calibrations are provided by the ST-ECF group in the configuration files for the aXe software. Two white dwarf standards were used to determine the flux calibration for both HRC and SBC prisms. The HRC/PR200L wavelength calibration has been secured with observations of the LMC PN SMP-79 and a quasar with both STIS and the ACS prism (Larsen et al. 2006). The calibration of the SBC/PR130L prism was determined using two quasars (Larsen 2006).

Background subtraction was performed during spectral extraction. To remove the sky background, a local background is estimated by interpolating between the adjacent pixels on either side of the target spectrum, outside the extracting area. The optimal weighting algorithm was chosen to enhance the signal-to-noise ratio of the extracted spectra. The algorithm assigns lower weights to pixels which contain only a small fraction of the target flux, due to the larger distance from the spectral trace.

Faint objects near the targets were identified by position and size, and then their contribution to the flux was subtracted in the extracted spectra. The contaminating flux from all other sources was estimated with a gaussian emission model by using the sizes and magnitudes derived from the direct image. This contamination flux was then subtracted when extracting the target spectrum.

The tabular wavelength and flux of the final extracted spectrum was then read using task `tprint` and converted to 1-d spectrum using the task `rspectext`. We averaged the multiple exposures using task `scombine`. The final reduced spectra of the 11 PNe are shown in Figure 1 to 11. The nebular line fluxes have been measured by integrating the area above the continuum using the IRAF task `splot` with the `d` or `w` options.

In Table 2 we give the complete spectral analysis of our targets, including the identification wavelength (column 2), the line ID (column 3), and the measured flux as a fraction of  $F_{H\beta}$  (column 4), where the  $H\beta$  fluxes are from the *HST* analysis of Stanghellini et al. (2003) and Shaw et al. (2006). It is worth noting that the emission around  $\lambda 1650$  could well be a blend of H II  $\lambda 1640$  and O III]  $\lambda 1663$  (the latter corresponding to the 1661/66 Å doublet). For those low- excitation PNe whose optical spectra do not show the  $\lambda 4686$  emission line (SMP 18, SMP 20, SMP 24) it is safe to assume that the emission is due to O III]. In the other cases we identify the emission as a blend. We do not calculate abundances of other elements than carbon in this paper, so we do not present here a detailed analysis of the other emission lines.

Typical uncertainties in the emission line fluxes are  $\sim 5\%$  in the bright lines. We have examined data quality flags of each exposure, and noticed that a few of the PR200L frames have some saturated pixels at the red end of their spectra. This is caused by red pile-up, due

to the low dispersion in the red wavelengths. In general the saturated pixels do not affect the measured fluxes. Only in two PNe, SMP 15 and SMP 18, the saturated pixels affect the C II]  $\lambda 2326$  emission line, therefore these are listed as lower limits.

Furthermore, in some cases the spectra are affected by bad pixels. For SMP 24, the 2D PR130L spectrum falls into an area of bad pixels, as indicated in the data quality file. If we exclude the bad pixels when extracting this spectrum we end up with a very marred 1D spectrum, thus the C IV  $\lambda 1550$  line measurement is not reliable for this nebula, even if there seems to be a feature at the appropriate wavelength. The PR200L spectrum looks much better, but the extension shows a dip on the C III]  $\lambda 1909$  line affecting the measured flux at an estimated level of 15% level. For SMP 16 the bad pixels in the PR200L frame affect the measured fluxes of the C II]  $\lambda 2326$  and C III]  $\lambda 1909$  lines at an estimated level of 25%. Finally, in the case of SMP 18 the C II]  $\lambda 2326$  flux might be affected at the 15% level. In the case of SMP 25 a prominent NIV]  $\lambda 1485$  is seen in the spectrum, but we do not give its flux in our tables since there are few columns of bad pixels 1425-1525Å range for this PN.

Ultraviolet prism spectroscopy performed with the ACS have not been acquired often in the past, and the analysis modes used in this paper are unique. In order to have a sanity check of our calibration and spectral extraction we compare the ACS prism HRC/PR200L spectrum of SMP 79, a PN in the LMC, with the corresponding spectrum observed with STIS spectroscopy. The prism spectrum was extracted in the same way as for our SMC PN targets. We measured the flux of C III]  $\lambda 1909$  to compare with the flux measured from the STIS spectrum. In the *HST* archive there are a total of 24 prism exposures of SMP 79 taken at 12 different positions of the CCD. We extracted the spectrum from each exposure, and measured the C III] flux in each spectrum. The average flux is  $(9.3 \pm 0.4) \times 10^{-13}$  [erg cm<sup>-2</sup> s<sup>-1</sup>], compared to the flux  $9.4 \times 10^{-13}$  [erg cm<sup>-2</sup> s<sup>-1</sup>] measured from the STIS spectrum. A contaminating source happened to lie just at the spectral trace of C II]  $\lambda 2326$ , so we did not attempt to compare this emission line with the one from STIS for LMC SMP 79. Errors in our flux measurements are  $\sim 5\%$  except the specific cases listed above, as marked in Table 2.

### 2.3. Extinction Correction

The flux measurements need to be corrected both for Galactic foreground extinction and for the SMC extinction proper. The relation between observed and de-reddened fluxes, scaled to H $\beta$ , can be written as

$$\frac{I_\lambda}{I_\beta} = \frac{F_\lambda}{F_\beta} 10^{cf_\lambda}, \quad (1)$$

where  $c$  is the target-dependent logarithmic extinction at  $H\beta$  and  $f_\lambda$  is the reddening function at wavelength  $\lambda$ . Since the Galaxy and the SMC have different extinction curves in the UV (Hutchings & Giasson 2001), we need to correct separately for each contribution. We can write:

$$cf_\lambda = c_G f_{\lambda,G} + c_{\text{SMC}} f_{\lambda,\text{SMC}}, \quad (2)$$

where the suffixes "G" and "SMC" refer to the Galactic foreground and intrinsic SMC extinction, respectively.

To evaluate the Galactic foreground extinction we used the Galactic H I foreground column density map constructed by Bot et al. (2004) from data of the the Parkes H I Survey of the Magellanic System (Brüns et al. 2005). The column density was obtained by integrating the emission from  $-60$  to  $+50$  km s $^{-1}$ , outside the SMC velocities. The Galactic color excess map is calculated using  $N(\text{H I}) / E_{B-V} = 5.8 \times 10^{21}$  [atoms cm $^{-2}$  mag $^{-1}$ ] (Bohlin et al. 1978; Savage & Mathis 1979). Figure 12 shows the Galactic foreground color excess map, superimposed to the Digital Sky Survey<sup>3</sup> image of SMC. The target-specific foreground Galactic extinction constant,  $c_G = 1.47 E_{B-V}$ , was estimated from Figure 13 for each target.

The constant  $c_G$  is then used to correct the fluxes for foreground Galactic extinction using the extinction function  $f_{\lambda,G}$  provided by Cardelli et al. (1989):

$$\left(\frac{I_\lambda}{I_\beta}\right)_0 = \frac{F_\lambda}{F_\beta} 10^{c_G f_{\lambda,G}} \quad (3)$$

In order to correct for the SMC extinciton we estimate the optical extinction constant as:

$$c_{\text{SMC}} = 2.875 \log \frac{(H\alpha/H\beta)_0}{2.85}, \quad (4)$$

where  $H\alpha/H\beta_0$  is the flux ratio corrected for Galactic foreground. We then correct the flux ratios for SMC extinction from:

$$\frac{I_\lambda}{I_\beta} = \left(\frac{I_\lambda}{I_\beta}\right)_0 10^{c_{\text{SMC}} f_{\lambda,\text{SMC}}} \quad (5)$$

where the SMC the extinction function is from Prevot et al. (1984). In Table 2 we list the Galactic (column 5) and SMC (column 6) extinciton constants, as calculated above, and the final corrected intensity ratios (column 7). Note that the line extinction estimated in the

---

<sup>3</sup>The Digitized Sky Surveys were produced at the Space Telescope Science Institute under U.S. Government grant NAG W-2166. The images of these surveys are based on photographic data obtained using the Oschin Schmidt Telescope on Palomar Mountain and the UK Schmidt Telescope. The plates were processed into the present compressed digital form with the permission of these institutions.



foreground overestimates the total line extinction in a few cases, thus the SMC extinction has been assumed to be zero.

## 2.4. Comparison to Previous Observations

While none of the observed targets had observations in the literature that allowed carbon abundance determination, several have UV spectra taken in comparable wavelength ranges, and limited comparison could be made among data sets. Let us examine these cases.

**SMP 6:** The FOS spectrum published by Vassiliadis et al. (1996) is deemed to be inadequate for precise flux measurements (see also SMP 28 below), thus we do not compare their fluxes to ours, although we do observe the same bright emission lines.

**SMP 15:** A low S/N IUE spectrum of this SMC PN, also known as N 43, has been acquired by Aller et al. (1987). The only emission line available in the 1200-1910 Å wavelength window is C III]  $\lambda$ 1909, with  $F_\lambda = 7 \times 10^{-13}$  [erg cm<sup>-2</sup>s<sup>-1</sup>], which is within  $\sim 10\%$  of our measurement.

**SMP 20:** Similarly to SMP 15, the only emission line measured by Aller et al. (1987) on the IUE spectrum of this SMC PN, also known as N 54, is C III]  $\lambda$ 1909, with  $F_\lambda = 7 \times 10^{-13}$  [erg cm<sup>-2</sup>s<sup>-1</sup>], which is also within  $\sim 10\%$  of our measurement.

**SMP 28:** The UV spectrum of this SMC PN short-ward of the C III]  $\lambda$ 1909 line is available from Meatheringham et al. (1990). Meatheringham et al. (1990) give flux values, and quote the flux error to better than 15% for brightest lines. By comparing the flux of the bright emission lines that we have in common, O IV]  $\lambda$ 1404, N IV]  $\lambda$  1487, He II  $\lambda$ 1640, and N III  $\lambda$ 1755, we found that they agree to better than the quoted errors for the two bluer lines, but the agreement gets worse for the redder lines measured in our PR130L spectrum. In addition to the IUE spectrum there is a FOS spectrum of this PN (Vassiliadis et al. 1996) whose fluxes are very uncertain, deemed to be systematically off by the authors. For this reason we will not compare our results with the FOS fluxes. We can use the FOS spectrum as presented by Vassiliadis et al. (1996) to confirm that they also observe the C III]  $\lambda$ 1909 emission line, contrary to what is derived from the IUE spectrum. Furthermore, the emission that we observe at 1553 Å is more likely to be associated with C IV than with Ne V, as suggested by Meatheringham et al. (1990). In summary, the statement that this PN is very carbon poor might not be correct in the light of our observations.

Finally, Idiart et al. (2007) used the IUE final archived spectra to measure the  $\lambda$ 1909 line for several of the PNe in our sample. The  $\lambda$ 1909 intensities by Idiart et al. (2007) carry

much larger uncertainties than ours, due to the low signal-to-noise ratio of the IUE spectra. All intensities agree with our data within the uncertainties, except for SMP 6, SMP 13, and SMP 18 where the IUE spectra are noisy and the errors quoted by Idiart et al. (2007) are very large. The IUE spectra would not provide the [C IV] nor the [C II] fluxes, thus their use to abundance analysis can only establish lower limits to the atomic abundances.

The comparison of the SMP 28 PR130L spectrum with that of Meatheringham et al. (1990) gives us confidence that the C IV] line flux that we measured is accurate. Overall, we do not have errors larger than 5-10% in this part of the spectrum. Furthermore, the comparison of the C III] emission lines of our PR200L observations with those by Aller et al. (1987) confirms that we have reliable measurements for all the carbon lines.

### 3. Abundance Analysis

The ionic abundances of  $C^+/H^+$  and  $C^{2+}/H^+$  were computed using the `nebular` package in STSDAS (Shaw & Dufour 1995; Shaw et al. 1998). We used the line intensities of Table 2, and  $T_e$  and  $N_e$  derived from the diagnostic lines measured by Shaw et al. (in preparation, hereafter SEA), if available, otherwise we used the plasma diagnostics by Leisy & Dennefeld (2006), hereafter LD06. In Table 3 we present the plasma diagnostics used in this paper; columns (2), (3), and (4) give respectively the low- and high-excitation  $T_e$  and the  $N_e$  used, column (5) lists the references for the spectral lines used to calculate the diagnostics, and column (6) gives the excitation class (EC) of the nebulae, which have been estimated accordingly to Morgan (1984).

The  $C^{3+}/H^+$  abundances must be derived from recombination lines, and we did so on the basis of approximate relations from Aller (1984) (Eq. 5.40). The ionic abundances for carbon are listed in Table 4, where columns (2), (3), and (4) give respectively the  $C^+$ ,  $C^{2+}$  and  $C^{3+}$  abundances in terms of hydrogen.

It is worth noting that, at our spectral resolution, the  $\lambda 2326$  emission line could have a [O III] component from the  $\lambda 2321$  emission. We calculate the volume emissivities for  $C^+$  and  $O^{2+}$ , the latter from the optical emission lines, for all PNe where  $\lambda 2326$  has been observed. We found that the ratio of the emission volumes between the carbon and oxygen transitions is typically  $\sim 50$  for the electron densities and temperatures of interest, thus the [O III] contribution does not affect our  $C^+$  ionic abundances.

In order to calculate the total carbon abundances we follow the discussion by Kingsburgh & Barlow (1994), also used by LD06. For low excitation PNe where the  $C^+$ ,  $C^{2+}$ , and  $C^{3+}$  abundances are available, the total carbon abundance can be calculate simply by summing

the ionic contribution. This is the case of SMP 13, SMP 15, SMP 16, SMP 18, and SMP 20, whose spectra do not show He II emission thus correction for  $C^{+4}$  would be unnecessary. This is also the case of SMP 6, whose emission around 1640-1663 Å should be due almost entirely to the [O III] component given the PN low optical excitation.

Next we need to calculate the ionization correction factors (ICFs) for the unseen ionization stages. We correct for the unseen  $C^+$  lines in SMP 8, SMP 24, SMP 25, SMP 26 and SMP 28 with Eqs. A11 and A13 (KB94). The ionic oxygen abundances used to obtain these ICFs have been calculated using the oxygen emission lines in SEA (SMP 8) and LD06, the plasma diagnostics of Table 3, and the `nebular` routines. As it turns out, no correction is needed for SMP 8. In SMP 25, SMP 26, and SMP 28 we do not see the  $C^+$  emission probably due to their high excitation. We still calculate the correction and implement the correction, as in LD96, but this has a marginal effect on the final carbon abundances for these PNe. We also calculated the ICFs to account for the unseen  $C^{4+}$  emission in the medium- to high-excitation PNe. For planetary nebulae SMP 25, SMP 26, and SMP 28, showing  $He^{2+}$  emission and not  $N^{4+}$  lines, we use Eq. A20 (KB94). The ionic helium abundances needed in these cases were calculated with the line intensities from LD06, the prescription of Benjamin et al. (1999), and the plasma diagnostics of Table 3.

The final ICFs are listed in column (5) of table 4, and the corrected abundances expressed in terms of  $A(C)=\log(C/H)+12$  are given in column (6), together with a conservative estimate of their uncertainties.

The larger factor of uncertainty for the total carbon abundances is the uncertainty in the electron temperature. The errors listed in Table 4 include the propagation of the uncertainty in the  $T_e$  for all ions, if the plasma diagnostics was available in SEA. For the other nebulae we estimate similar errors in the  $T_e$  and propagate the errors, as given in Table 4, unless there are other, larger uncertainties, as discussed below.

As reported in Table 2 the  $C^{2+}$  fluxes of SMP 15 and SMP 18 are lower limits; we estimate that the total carbon abundances calculated for these two PNe might be underestimated by  $\sim 5\%$ .

Finally, while most of the emission lines intensities have errors  $\sim 5\%$ , they go up to 15 and 25% respectively in SMP 24 and SMP 16. These errors are propagated through the carbon abundance analysis.

By considering the sample of this paper and the other carbon abundances in the literature, including only those who consider all the present excitation levels (Aller 1987; LD06), we found that  $\langle C/H \rangle_{SMC}=(3.75\pm 3.64)\times 10^{-4}$ . This is  $\sim 1.5$  times higher than the same average for the LMC ( $\langle C/H \rangle_{LMC}=(2.49\pm 2.18)\times 10^{-4}$ , Stanghellini et al. 2005).

#### 4. Magellanic Cloud PNe and the stellar evolution models

Carbon, the fourth most abundant element in the Universe (Clayton 2003), is vigorously produced in LIMS, thus it probes their evolution. The  $\alpha$ -elements (oxygen, neon, argon and sulfur), on the other hand, are produced by nucleosynthesis of Type II supernova and provide information about the original composition of the PN progenitor at the time of birth. Oxygen may be brought up to the LIMS surface by the third dredge-up, and its abundance should be used cautiously in this capacity.

We use the SMC PN carbon abundances determined in this paper, and those available in the literature, and relate them to the abundance of the  $\alpha$ -elements, to assess the models of stellar evolution and the theoretical yields. In order to compare populations of different metallicity we also include in the plots the results from our study of carbon abundances in the LMC PNe (Stanghellini et al. 2005). The abundances of N, O, and Ne for LMC PNe used here are from Aller et al. (1987), and Leisy & Dennefeld (1996, 2006). Corresponding values of N, O, and Ne in SMC PNe come from Leisy & Dennefeld (1996), and SEA.

In Fig. 13 we show the carbon vs. oxygen abundances<sup>4</sup> of PNe in the SMC (filled symbols) and the LMC (open symbols). Their morphologies are indicated by symbols of various shapes. Small symbols are used for PNe of unknown morphologies, i. e., not yet observed with *HST* or, in a couple of cases, where the morphological class was too uncertain to be assigned. Abundances are in the usual scale of  $A(X)=\log(X/H)+12$ . The PNe separate into two groups: The first group are those with  $C/O < 1$  (below the line), whose shapes are almost exclusively bipolar or bipolar core (BC<sup>5</sup>), as already noted in Stanghellini et al. (2007); these PNe are associated with relatively young stellar populations, such as the disk of the Milky Way. And the second group are those with  $C/O > 1$ , corresponding to the less massive progenitors. Most of the SMC PNe lie in the  $C/O > 1$  part of this plot.

The predominance of C-rich PNe in the SMC is consistent with the theoretical expectation that the third dredge-up is predicted to be favored at lower metallicity, i. e., to occur in stars of lower masses and with a higher efficiency (e. g., Karakas, Lattanzio, & Pols 2002; Stancliffe et al. 2005). Carbon is converted to nitrogen by hot-bottom burning (HBB). HBB is likely active only in relatively high-mass AGB stars ( $M_{\text{HBB}}^{\text{min}} \sim 3.5\text{--}5 M_{\odot}$ , depending on

---

<sup>4</sup>For the sake of clarity we do not plot carbon abundance error bars, that are given in Table 4. Note that uncertainties of  $\sim 10\%$  would be within the symbol size.

<sup>5</sup>PNe with BC morphologies are those with pinched or barrel-shaped cores similar to known bipolars with protruding lobes. This classification is somewhat ambiguous and may include some PNe with unusual shapes, and some misclassified elliptical PNe.

metallicity ) with very deep convection and hot cores (Marigo 2001). Star formation has been far more active in the gas-rich LMC than in the gas-depleted SMC. Possibly, many of the PNe that have formed in the LMC have higher average masses than those in the SMC, affecting the fraction of high-end mass LIMS that will go through the HBB phase. That is, the segregation of PNe with bipolar and BC symmetries below the C=O line is fully consistent with model calculations. It is worth recalling, in fact, that Villaver (2004) found a lack of intermediate-mass central stars in the SMC, present in the LMC.

SMC SMP 22 and SMC SMP 25 are two exceptions to this scenario. They are the two morphologically unclassified SMC PNe in the lower-left of the plot: low metallicity (LD06) and  $C/O < 1$ . Not much is known about SMP 22. SMP 25 is quite unique among SMC PNe. It is the only PN in the SMC where oxygen-rich dust has been detected (Stanghellini et al. 2007), while all other SMC PNe observed with Spitzer/IRS have carbon-rich dust. Furthermore, the central star of SMP 25 is much more massive ( $M \sim 0.82 M_{\odot}$ , Villaver et al. 2004) than the typical central in Magellanic Cloud PNe (Villaver et al. 2007), and it is located in the eastern region of the SMC facing the LMC, a region that contains younger and more metal rich clusters (Crowl et al. 2001) and where Dopita et al. (1985) found the kinematically younger PNe to be concentrated. SMP 25 may have undergone recent HBB activity.

In Figure 14, where we show the relation between  $C/O$  and the neon abundance, we confirm the carbon-abundance segregation of SMC PNe. There is no evidence that neon's abundance has been modified in any way, nor that the  $C/O$  ratio is modified differently in the SMC than in the LMC depending on the initial neon.

The  $\log(O/N)$  vs.  $\log(C/N)$  plot (Fig. 15) also shows some obvious and interesting groupings of data. The segregation of bipolar nebulae on the left side of the plotted line is expected of course, since figures 13 and 15 are not entirely independent. However, it is clear that the bipolar that exhibit  $O > C$  also have  $N > C$ : that is, they are "N rich". Symbiotic stars and novae stars (not shown; Nussbaumer et al. 1988) are also found in the same region. On the other hand, all of the sample with  $C/O > 1$  from Fig. 13 are also nitrogen poor; that is,  $N < O$  and  $N < C$ . Most of the SMC PNe fall into the latter group, of course. Carbon stars (not shown; Nussbaumer et al. 1988) are also found in this region.

Carbon stars probably have not undergone any HBB processing. We can compare the data in Fig. 15 with the yields from models of stellar evolution. We limit our comparison to the final yields calculated by Marigo (2001), to avoid overcrowding of the plot. The yields by van den Hoek & Groenewegen (1997) or Karakas & Lattanzio (2007) would look very similar to the ones by Marigo (2001) on this plot. We indicate the yields from LIMS evolution with starred symbols: the four-pointed stars correspond  $Z=0.008$  while the six-

pointed stars are for  $Z=0.004$ , and we used smaller symbols for stars with progenitor masses too low to have undergone the HBB ( $M_{\text{HBB}}^{\text{min}} \sim 3.5$  and  $4.0 M_{\odot}$  for the SMC, and the LMC models respectively, as in Marigo 2001). The abundance ratios measured for round and elliptical PNe correspond very well with the final yields predicted for the evolution of the lower mass-end of LIMS in both the SMC and the LMC. Similarly, the *massive* models are in good agreement with the abundance ratios of C, N, and O in the PNe in the LMC with bipolar and BC morphologies. These results are extremely satisfying verifications of difficult model predictions. In Figure 16 we plot the sum of carbon, oxygen, and nitrogen abundances vs. carbon of LMC and SMC PNe. Fig.16 is a classical diagram for assessing the efficiency of CNO-cycling. The CNO abundance would be preserved if these elements were only acting as catalysts, while carbon enhancement via third dredge up is clearly present in the SMC PNe.

Based on a study of LMC and SMC optical lines, Stanghellini et al. (2003) found that the observed intensity ratio  $I_{[\text{OIII}]\lambda 5007}/I_{\text{H}\beta}$  seems to increase with metallicity. The photoionization models in Stanghellini et al. (2003) show that metallicity impacts the relative emission line strength of the major coolants, and that the UV carbon emission lines have a significant effect in cooling PNe with low metallicities. Now that we have observations of carbon emission lines in both SMC and LMC PNe we can assess the validity of those models. In Fig.17 we plot the histogram of the  $I_{\lambda 5007}/I_{\lambda 1909}$  line intensity ratio for the SMC (thick line) and the LMC (thin, shaded histogram) PNe. The distributions, which have been normalized for the number of PNe in each sample, appear to be different at very low and very high intensity ratios, indicating that the carbon emission line is a very important coolant for most SMC PNe. We calculate that the average line intensity ratio is 6.23 and 2.36 respectively for the LMC and SMC PNe, and the median values of  $I_{\lambda 5007}/I_{\lambda 1909}$  are  $3.34 \pm 2.98$  and  $1.83 \pm 0.83$  for the LMC and the SMC PNe respectively, marking a sharp difference in the dominant cooling agents at different metallicities. The carbon  $\lambda 1909$  line is a much more efficient coolant, with respect to the  $\lambda 5007$  line, in the SMC than the LMC PNe, The CIV line can also be an important coolant in the low-metallicity, highly ionized PNe.

## 5. Conclusions

The present paper provides a database of 11 SMC PNe whose carbon abundance has been accurately derived through prism spectroscopy with the ACS/*HST*. The number of reliable SMC PNe with well-measured carbon abundances has doubled, finally allowing statistically useful analysis of carbon production and CNO-cycling in PNe at the very low metallicity in the progenitors of SMC PNe.

By comparing the abundances of SMC and LMC PNe we found that most observed SMC PNe are carbon rich, except in a couple of unusual cases, SMP 22 and SMP 25, where there is indication that the progenitors underwent the HBB process. This seems to indicate that most SMC PNe derive from low-mass ( $M_{\text{to}} < 3.5 M_{\odot}$ ) and low-metallicity progenitors. By comparison, the LMC has a much varied PN population, where both carbon-rich and carbon-depleted PNe are present, indicating a larger range of PN progenitor mass and metallicity, including several PNe whose progenitors could be in the 3-5  $M_{\odot}$  mass range. While a larger SMC PN sample would improve the impact of these findings, it is worth recalling that both LMC and SMC samples were selected homogeneously, and that with the present observations we have increased the statistical significance of the SMC PN sample to almost the same level of confidence as the LMC sample (Shaw et al. 2006).

The CNO abundances in Magellanic Cloud PNe can now be used to test the predictions of models of stellar evolution. We found that the data agree impressively with the final yields from Marigo (2001) models, calculated both for the SMC and LMC metallicities. In particular, the yields calculated for turnoff mass  $< 3.5$ , and  $4.0 M_{\odot}$  seem to reproduce PN abundances of round and elliptical PNe in the SMC, and in the LMC, respectively. Yields from the more massive LIMS encompass well the bipolar PNe abundances. If we accept the model results then the production of carbon through the CNO cycle in the SMC PNe shows that most SMC PN progenitors are in the low-mass end of the LIMS mass range, while the LMC PNe could have progenitors in the whole LIMS range. In some cases extra-mixing or other process that were not included in the current models are needed to justify the observed CNO abundances.

Compared to the SMC, the LMC has been a site of recent or ongoing star formation and heavy-element enrichment. One of the most important results of our study is that the average abundance of carbon in SMC PNe is  $\sim 1.5$  times higher than the average carbon measured in LMC PNe. Using the Magellanic Cloud sample of PNe with determined carbon abundances, and whose IRS/Spitzer spectra allows a determination of the dust chemistry (Stanghellini et al. 2007) we find that  $\langle C/H \rangle = (4.69 \pm 3.33) \times 10^{-4}$  for Magellanic Cloud PNe with carbon-rich dust. This is  $\sim 35$  times greater than the same ratio for PN with oxygen-rich dust,  $\langle C/H \rangle = (1.35 \pm 0.88) \times 10^{-5}$ , confirming a strong correlation between dust and gas chemistry.

The present observations also show that the high-excitation carbon emission lines are major or dominant coolants in the low metallicity SMC PNe, as predicted by Stanghellini et al. (2003), much more so than in LMC PNe, where the C III]  $\lambda 1909$  line intensity is typically a small fraction of the [O III]  $\lambda 5007$  line strength.

## 6. Acknowledgements

We thank Mark Dickinson for his help in modeling the prism response during the ACS phase II. Thanks are due to an anonymous Referee for important suggestions. Support for this work was provided by NASA through grant GO-10250.01-A from Space Telescope Science Institute, which is operated by the Association of Universities for Research in Astronomy, Inc., under NASA contract NAS5-26555.

## REFERENCES

- Aller, L. H. 1984, *Physics of Thermal Gaseous Nebulae* (Dordrecht: Reidel)
- Aller, L. H., Keyes, C. D., Maran, S. P., Gull, T. R., Michalitsianos, A. G., & Stecher, T. P. 1987, *ApJ*, 320, 159
- Benjamin, R. A., Skillman, E. D., & Smits, D. P. 1999, *ApJ*, 514, 307
- Bertin, E., & Arnouts, S. 1996, *A&AS*, 117, 393
- Bohlin, R. C., Savage, B. D., & Drake, J. F. 1978, *ApJ*, 224, 132
- Bot, C., Boulanger, F., Lagache, G., Cambr esy, L., & Egret, D. 2004, *A&A*, 423, 567
- Br uns, C., et al. 2005, *A&A*, 432, 45
- Cardelli, J. A., Clayton, G. C., & Mathis, J. S. 1989, *ApJ*, 345, 245
- Clayton, D. 2003, *Handbook of Isotopes in the Cosmos*, by Donald Clayton, pp. 326. ISBN 0521823811. Cambridge, UK: Cambridge University Press, October 2003.,
- Crowl, H. H., Sarajedini, A., Piatti, A. E., Geisler, D., Bica, E., Clari a, J. J., & Santos, J. F. C., Jr. 2001, *AJ*, 122, 220
- Dopita, M. A., Lawrence, C. J., Ford, H. C., & Webster, B. L. 1985, *ApJ*, 296, 390
- Hutchings, J. B., & Giasson, J. 2001, *PASP*, 113, 1205
- Idiart, T. P., Maciel, W. J., & Costa, R. D. D. 2007, *A&A*, 472, 101
- Iben, I., Jr., & Renzini, A. 1983, *ARA&A*, 21, 271
- Karakas, A., & Lattanzio, J. C. 2007, *Publications of the Astronomical Society of Australia*, 24, 103



- Kümmel, M., Walsh, J., Larson, S. & Pirzkal, N. 2005, aXe User Manual, Version 1.50
- Larsen, S. S. 2006, Wavelength and Flux Calibration of the ACS/SBC PR110L and Pr130L Prisms, ST-ECF Instrument Science Report ACS-2006-02
- Larsen, S. S., Walsh, J., & Kümmel, M. Wavelength and Flux Calibration of the ACS/HRC PR200L Prism, ST-ECF Instrument Science Report ACS-2006-3
- Leisy, P., & Dennefeld, M. 1996, *A&AS*, 116, 95
- Leisy, P., & Dennefeld, M. 2006, *A&A*, 456, 451 (LD06)
- Marigo, P. 2001, *A&A*, 370, 194
- Marigo, P., & Girardi, L. 2007, *A&A*, 469, 239
- Meatheringham, S. J., Maran, S. P., Stecher, T. P., Michalitsianos, A. G., Gull, T. R., Aller, L. H., & Keyes, C. D. 1990, *ApJ*, 361, 101
- Morgan, D. H. 1984, *MNRAS*, 208, 633
- Nussbaumer, H., Schmid, H. M., Vogel, M., & Schild, H. 1988, *A&A*, 198, 179
- Pavlovsky, C. et al. 2004, ACS Data Handbook, Version 3.0 (Baltimore: STScI)
- Prevot, M. L., Lequeux, J., Prevot, L., Maurice, E., & Rocca-Volmerange, B. 1984, *A&A*, 132, 389
- Savage, B. D., & Mathis, J. S. 1979, *ARA&A*, 17, 73
- Shaw, R. A., de La Pena, M. D., Katsanis, R. M., & Williams, R. E. 1998, in ASP Conf. Ser. 145, *Astronomical Data Analysis Software and Systems VII*, eds. R. Albrecht, R. N. Hook, & H. A. Bushouse (San Francisco: ASP), 192
- Shaw, R. A., & Dufour, R. J. 1995, *PASP*, 107, 896
- Shaw, R. A., Stanghellini, L., Villaver, E., & Mutchler, M. 2006, *ApJS*, in press
- Shaw, R. A. 2006, *Planetary Nebulae in our Galaxy and Beyond*, 234, 305
- Stanghellini, L., Shaw, R. A., Balick, B., Mutchler, M., Blades, J. C., & Villaver, E. 2003, *ApJ*, 596, 997
- Stanghellini, L., Shaw, R. A., & Gilmore, D. 2005, *ApJ*, 622, 294

Stanghellini, L., García-Lario, P., García-Hernández, D. A., Perea-Calderón, J. V., Davies, J. E., Manchado, A., Villaver, E., & Shaw, R. A. 2007, *ApJ*, 671, 1669

van den Hoek, L. B., & Groenewegen, M. A. T. 1997, *A&AS*, 123, 305

Vassiliadis, E., et al. 1996, *ApJS*, 105, 375

Villaver, E., Stanghellini, L., & Shaw, R. A. 2004, *ApJ*, 614, 716

Villaver, E., Stanghellini, L., & Shaw, R. A. 2007, *ApJ*, 656, 831

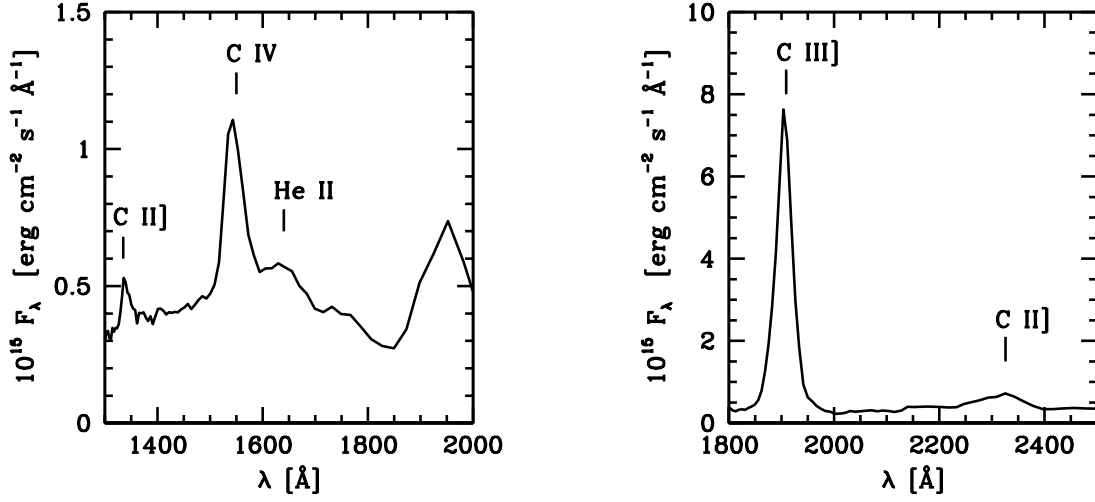


Fig. 1.— The extracted spectra from the PR130L (left panel) and PR200L (right panel) prism observations in SMP 6.

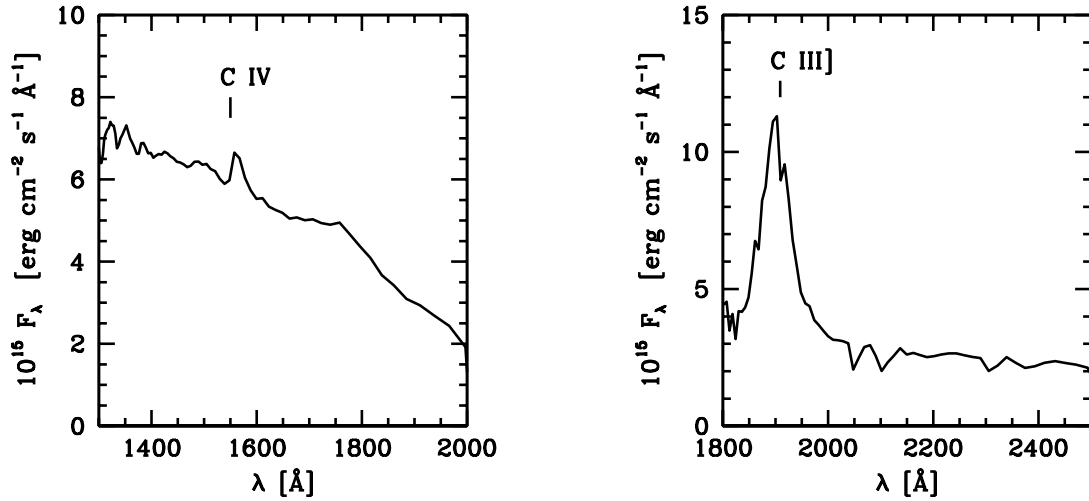


Fig. 2.— As in Figure 1, for SMP 8.

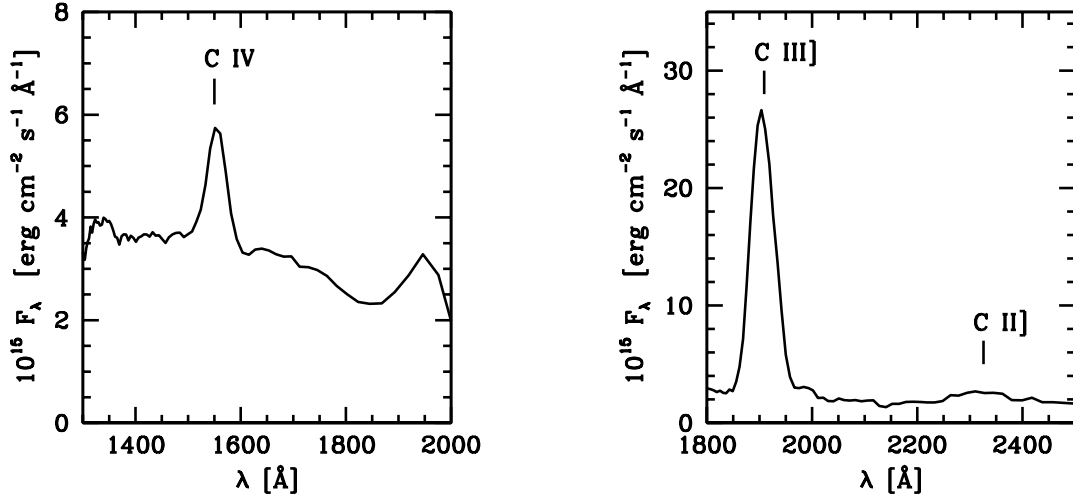


Fig. 3.— As in Figure 1, for SMP 13.

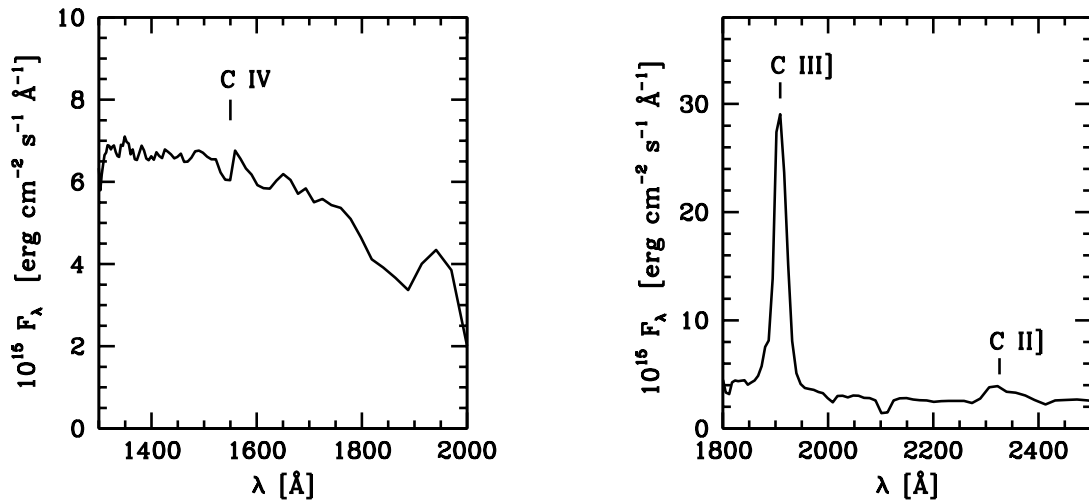


Fig. 4.— As in Figure 1, for SMP 15.

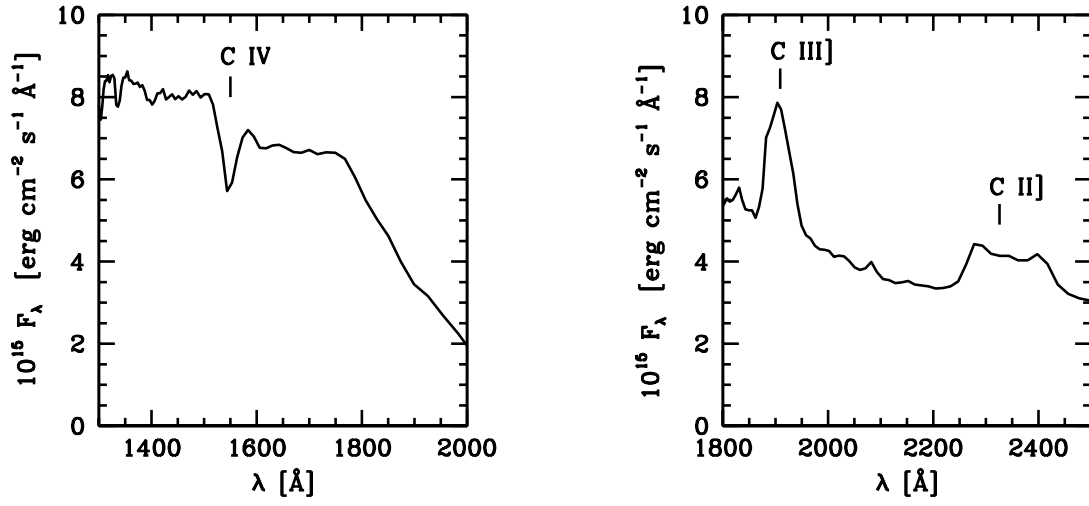


Fig. 5.— As in Figure 1, for SMP 16.

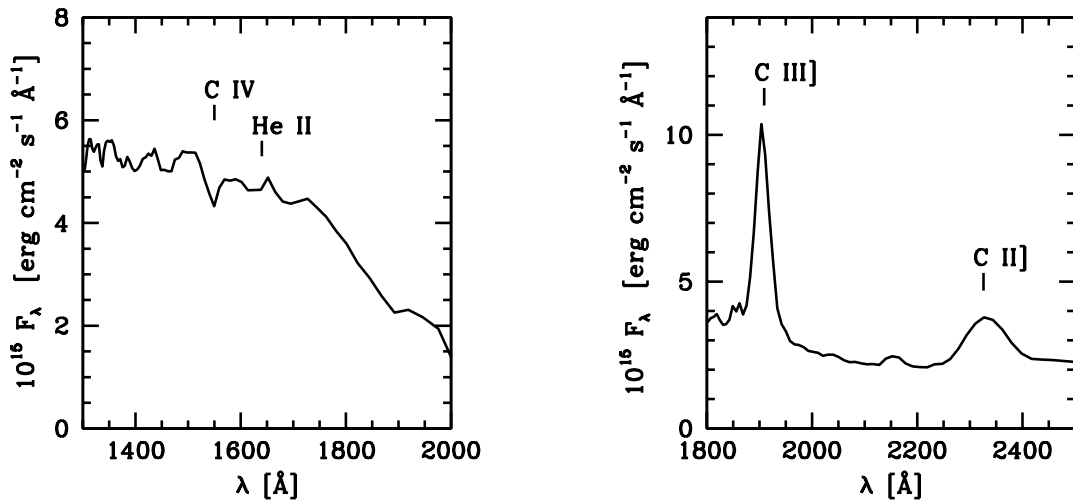


Fig. 6.— As in Figure 1, for SMP 18.

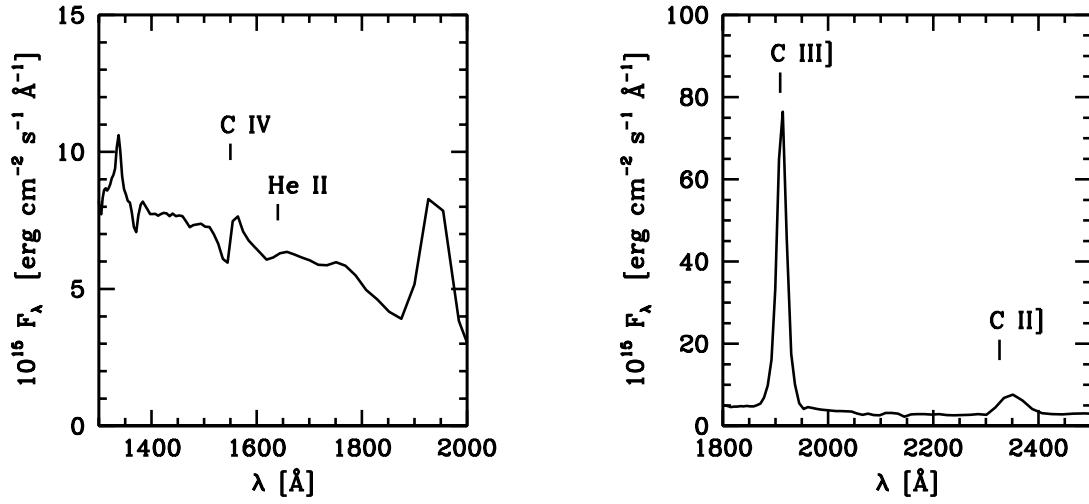


Fig. 7.— As in Figure 1, for SMP 20.

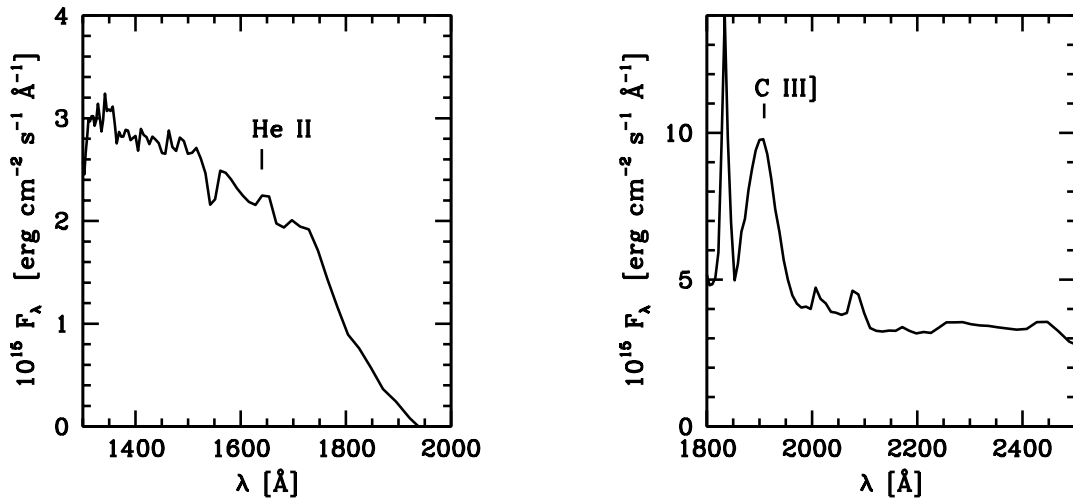


Fig. 8.— As in Figure 1, for SMP 24.

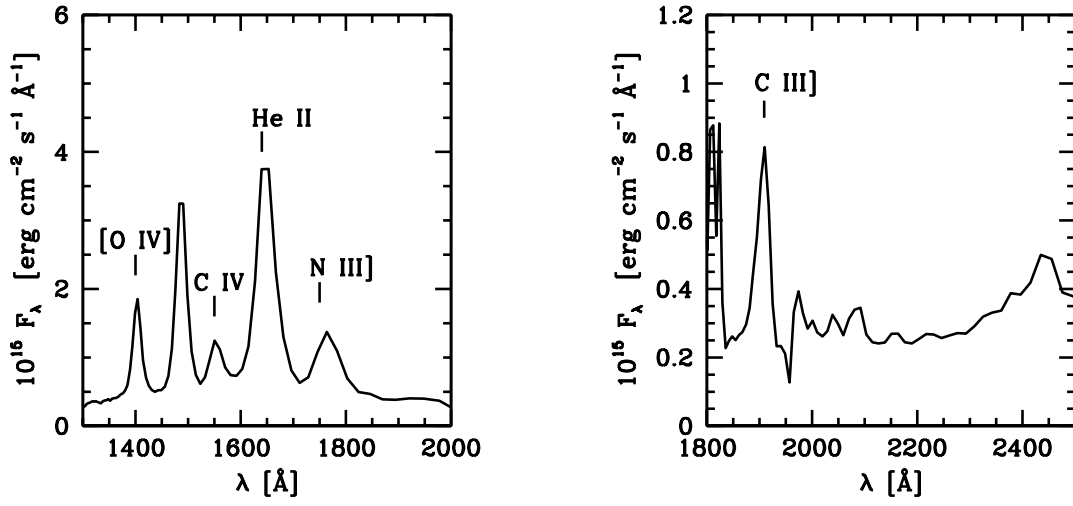


Fig. 9.— As in Figure 1, for SMP 25.

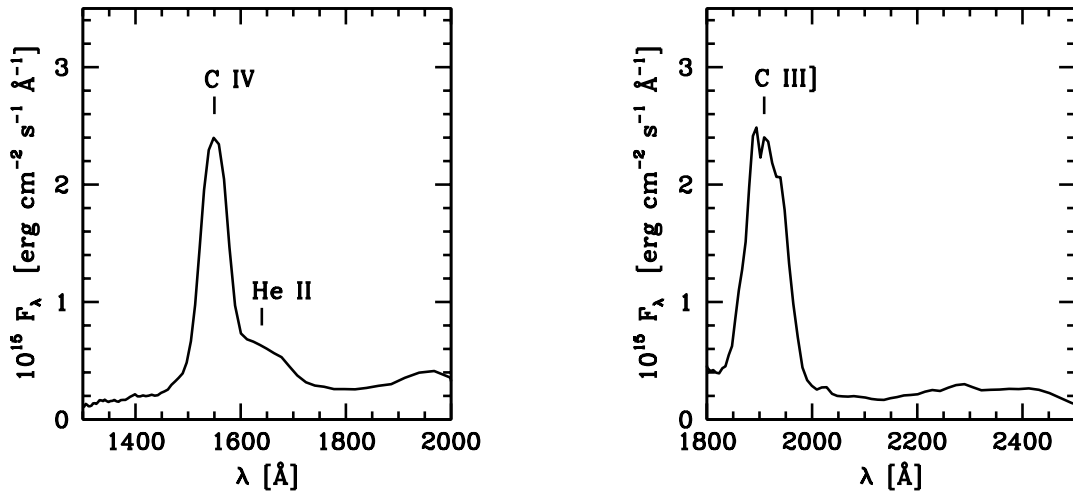


Fig. 10.— As in Figure 1, for SMP 26.

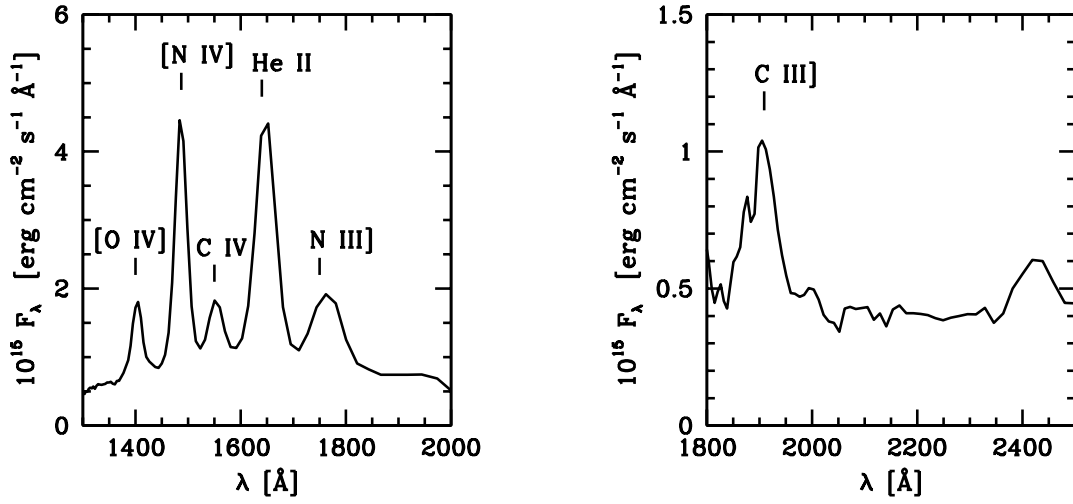


Fig. 11.— As in Figure 1, for SMP 28.



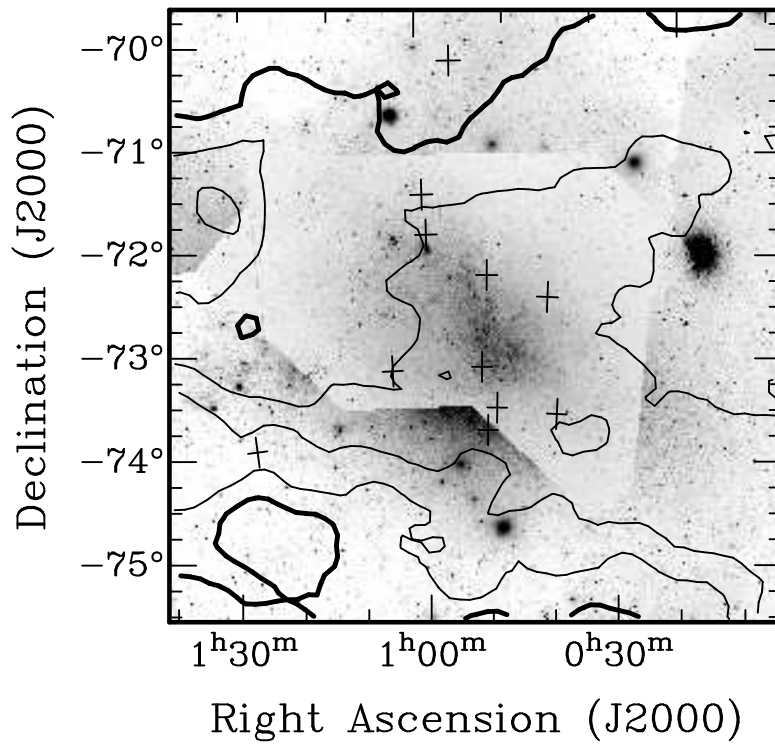


Fig. 12.— The contours represent the Galactic foreground color excess map towards the SMC are overlapped on the the Digital Sky Survey image of SMC. The contours represent  $E_{B-V}$  between 0.04<sup>m</sup> and 0.08<sup>m</sup> from top to bottom, plotted for every 0.01<sup>m</sup> interval, with the 0.04 and 0.08 contours marked in thick lines. The positions of our targets are indicated with crosses.

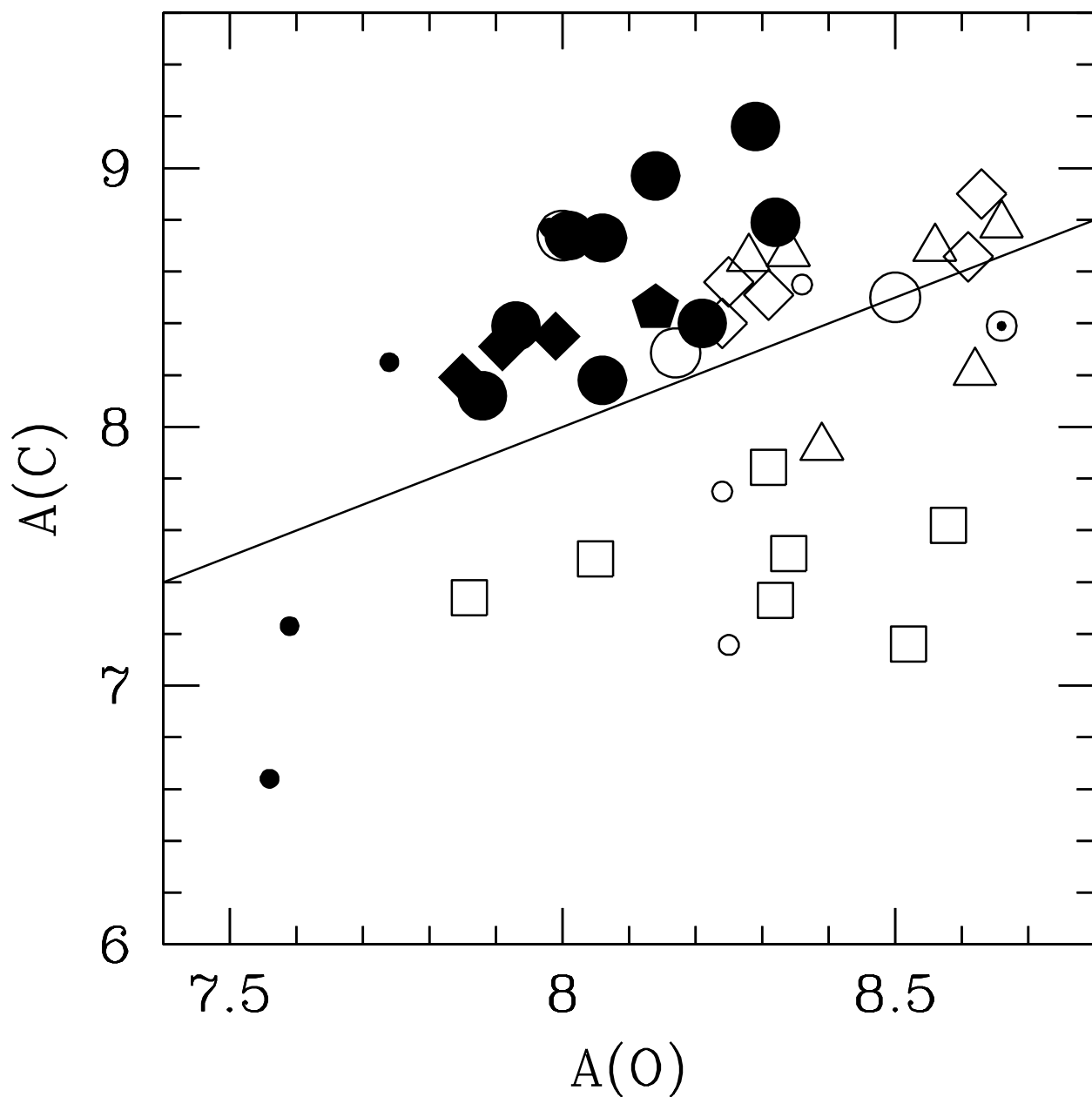


Fig. 13.— The distribution of SMC (filled symbols) and LMC (open symbols) PNe on the  $\log(C/H) - \log(O/H)$  plane. Symbol shapes represent the different morphologies. Circles: Round, diamonds: Elliptical, triangles: Bipolar core, squares: Bipolar, pentagons: Point-symmetric PNe. Small circles refer to unknown morphology, see text. The thick solid line represents the 1:1 correlation. The solar symbol indicates the abundances from Asplund et al. (2005).

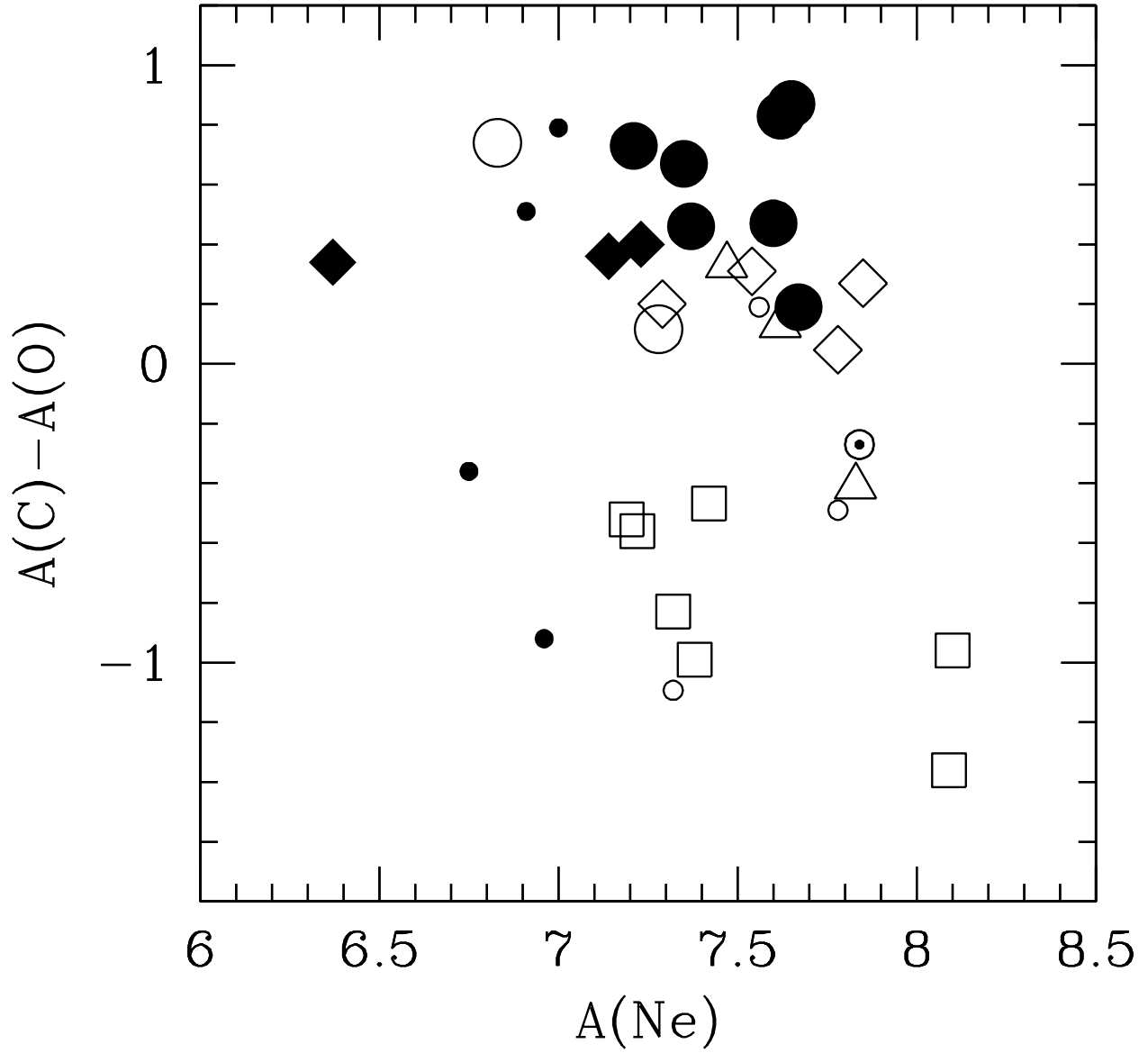


Fig. 14.— The distribution of SMC and LMC PNe on the  $\log(C/O) - \log(Ne/H)$  plane. Symbols are used as in Fig. 13

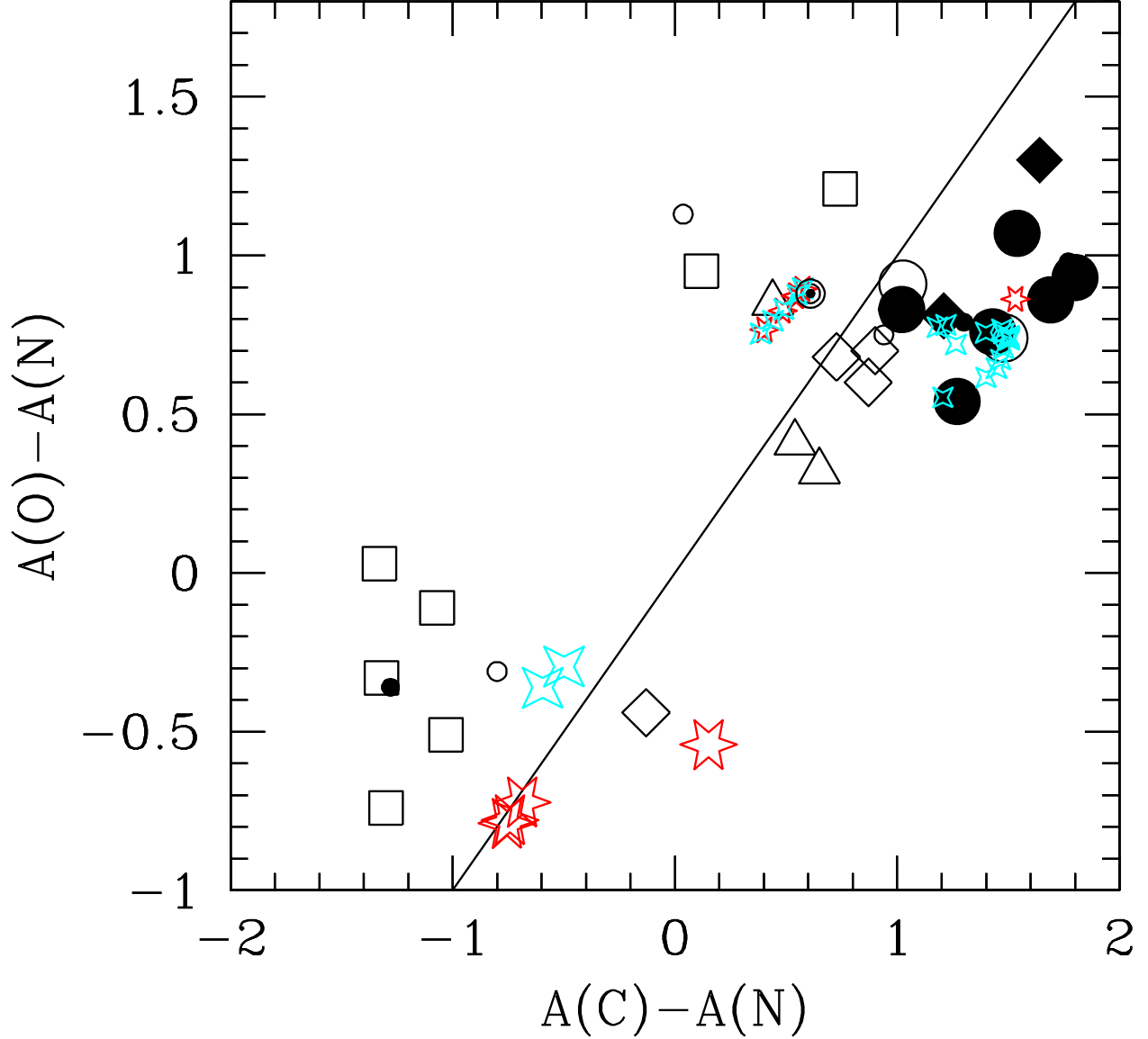


Fig. 15.— The distribution of SMC and LMC PNe on the  $\log(\text{C}/\text{N}) - \log(\text{O}/\text{N})$  plane. Symbols for data are used as in Fig. 13. The starred symbols represent the yields from stellar evolution by Marigo (2001), where the four-points stars are for the LMC and six-points stars are for the SMC PNe. Within the same set of models, different points indicate different initial mass, and the smaller symbols represent the yields from the evolution of  $M_{\text{to}} < M_{\text{HBB}}^{\text{min}}$ . The sun locus would be at (0.61; 0.88) in this plot, but it is not marked to avoid overlap with a target and few model points.

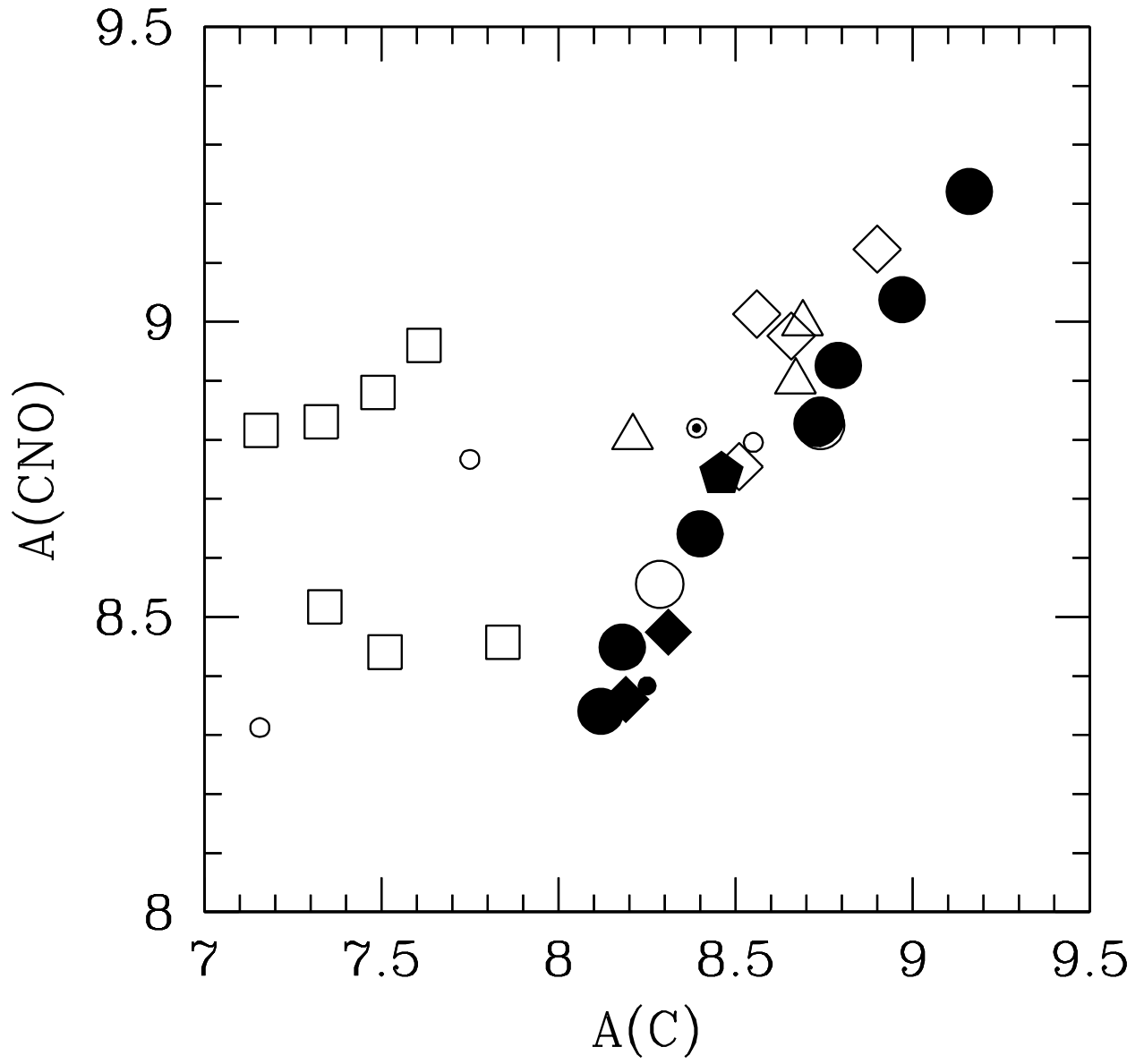


Fig. 16.— SMC and LMC PN abundance sum of C, N, and O vs. carbon abundance. Symbols are as in Fig. 13.

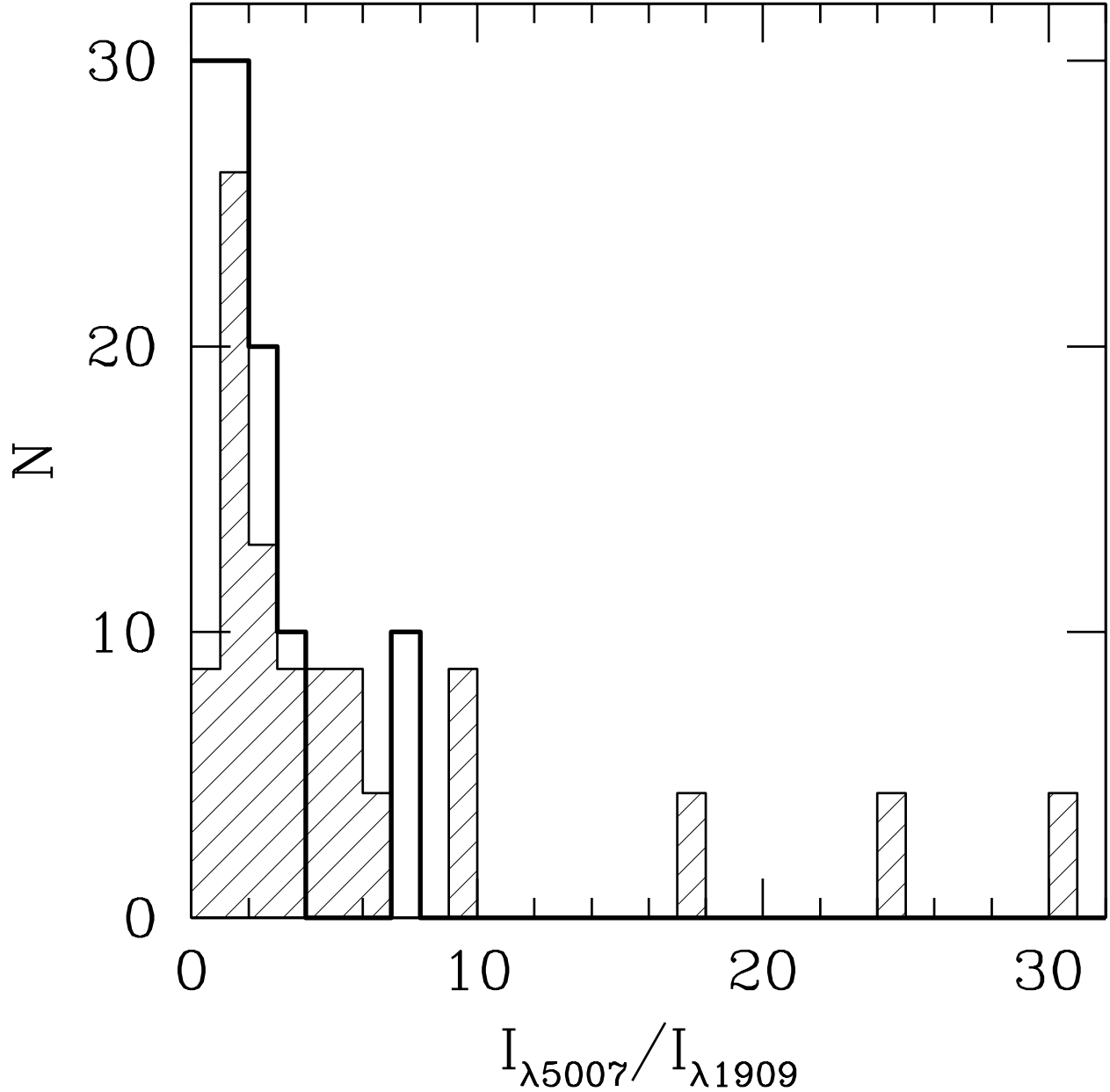


Fig. 17.— Cooling of SMC and LMC PNe through the major emission lines. The  $I_{\lambda 5007} / I_{\lambda 1909}$  histogram is shown for the SMC (heavy line) and the LMC (light shaded histogram) PNe. Note the very different distributions for  $I_{\lambda 5007} / I_{\lambda 1909} < 1$  and  $> 6$ .

Table 1. Observing logs

Name	Data Set	Observation Date	Setup	$t_{exp}$ (s)
SMP 6	j90d01011	2005 May 03	HRC/PR200L	2656
	j90d01f7q	2005 May 03	HRC/F330W	360
	j90da1fbq	2005 May 03	SBC/PR130L	2825
	j90da1faq	2005 May 03	SBC/F165LP	360
SMP 8	j90d02011	2006 Jan 18	HRC/PR200L	2716
	j90d02kjg	2006 Jan 18	HRC/F330W	300
	j90da2kmg	2006 Jan 19	SBC/PR130L	2820
	j90da2knq	2006 Jan 19	SBC/F165LP	360
SMP 13	j90d03021	2005 Aug 05	HRC/PR200L	2656
	j90d03011	2005 Aug 05	HRC/F330W	306
	j90da3y4q	2005 Aug 05	SBC/PR130L	2820
	j90da3y5q	2005 Aug 5	SBC/F165LP	360
SMP 15	j90d04011	2005 May 03	HRC/PR200L	2656
	j90d04fiq	2005 May 03	HRC/F330W	360
	j90da4fmq	2005 May 03	SBC/PR130L	2820
	j90da4flq	2005 May 03	SBC/F165LP	360
SMP 16	j90d05011	2005 Oct 01	HRC/PR200L	2656
	j90d05saq	2005 Oct 01	HRC/F330W	360
	j90da5sdq	2005 Oct 01	SBC/PR130L	2829
	j90da5seq	2005 Oct 01	SBC/F165LP	360
SMP 18	j90d06011	2005 Feb 14	HRC/PR200L	2656
	j90d06drq	2005 Feb 14	HRC/F330W	360
	j90d16p2q	2006 Jan 12	SBC/PR130L	2640
	j90d16p9q	2006 Jan 12	SBC/F165LP	300
SMP 20	j90d07011	2005 Apr 22	HRC/PR200L	2656
	j90d07aoq	2005 Apr 22	HRC/F330W	360
	j90da7arq	2005 Apr 22	SBC/PR130L	2820
	j90da7asq	2005 Apr 22	SBC/F165LP	360
SMP 24	j90d10011	2006 Sep 03	HRC/PR200L	2656
	j90d10aqq	2006 Sep 03	HRC/F330W	360

Table 1—Continued

Name	Data Set	Observation Date	Setup	$t_{exp}$ (s)
	j90da0atq	2006 Sep 03	SBC/PR130L	2825
	j90da9auq	2006 Sep 03	SBC/F165LP	360
SMP 25	j90d08u5q	2006 Sep 01	HRC/PR200L	2702
	j90d08u6q	2006 Sep 01	HRC/PR200L	3306
	j90d09u4q	2006 Sep 01	HRC/F330W	360
	j90da8010	2006 Sep 01	SBC/PR130L	6142
	j90da8u9q	2006 Sep 01	SBC/F165LP	360
SMP 26	j90d09s4q	2005 Sep 30	HRC/PR200L	2702
	j90d09s5q	2005 Sep 30	HRC/PR200L	3305
	j90d09s3q	2005 Sep 30	HRC/F330W	360
	j90da9010	2005 Oct 01	SBC/PR130L	6137
	j90da9s8q	2005 Oct 01	SBC/F165LP	360
SMP 28	j90d11011	2005 Aug 02	HRC/PR200L	2656
	j90d11gsq	2005 Aug 02	HRC/F330W	360
	j90db1gvq	2005 Aug 02	SBC/PR130L	2820
	j90db1gwq	2005 Aug 02	SBC/F165LP	360



Table 2. Spectral analysis

Name	$\lambda$	ID	$F_{\lambda}^a$	$c_G$	$c_{SMC}$	$I_{\lambda}^a$
SMP 06	1335	C II]	2.73	0.078	0.320	42.37
	1550	C IV	20.25	0.078	0.320	156.10
	1640-1663	He II,O III]	9.15	0.078	0.320	60.62
	1909	C III]	184.20	0.078	0.320	852.60
	2326	C II]	19.12	0.078	0.320	57.88
SMP 08	1550	C IV <sup>b</sup>	16.98	0.026	0.00	18.29
	1909	C III]	298.90	0.026	0.00	323.32
SMP 13	1550	C IV	40.46	0.076	0.130	104.80
	1909	C III]	501.90	0.076	0.130	1062.00
	2326	C II]	34.82	0.076	0.130	62.84
SMP 15	1550	C IV <sup>b</sup>	2.45	0.01	0.00	2.52
	1909	C III]	221.00	0.01	0.00	227.8
	2326	C II]	$\geq 31.85$	0.01	0.00	$\geq 32.82$
SMP 16	1550	C IV <sup>b</sup>	6.43	0.03	0.00	7.01
	1909	C III]	89.03 <sup>c</sup>	0.03	0.00	97.47
	2326	C II]	93.97 <sup>c</sup>	0.03	0.00	102.82
SMP 18	1550	C IV	0.68	0.076	0.058	1.17
	1663	O III	2.96	0.076	0.058	4.90
	1909	C III]	113.80	0.076	0.058	179.20
	2326	C II]	$\geq 62.16$	0.076	0.058	$\geq 92.37$
SMP 20	1550	C IV <sup>b</sup>	6.88	0.00	0.00	6.88
	1663	O III]	5.93	0.00	0.00	5.93
	1909	C III]	528.30	0.00	0.00	528.3
	2326	C II]	87.06	0.00	0.00	87.06
SMP 24	1663	O III]	2.18	0.047	0.00	2.49
	1909	C III]	147.60 <sup>d</sup>	0.047	0.00	168.43
SMP 25	1397-1407	[O IV]	65.93	0.069	0.042	109.10
	1550	C IV	68.02	0.069	0.042	104.40
	1640-1663	He II ,O III]	337.30	0.069	0.042	504.40
	1750	N III]	106.50	0.069	0.042	155.10

Table 2—Continued

Name	$\lambda$	ID	$F_{\lambda}^a$	$c_G$	$c_{SMC}$	$I_{\lambda}^a$
	1909	C III]	31.06	0.069	0.042	44.87
SMP 26	1550	C IV	509.50	0.075	0.190	1853.00
	1640-1663	He II, O III]	158.20	0.075	0.190	524.10
	1909	C III]	703.40	0.075	0.190	1895.00
SMP 28	1397-1407	[O IV]	36.48	0.098	0.041	65.49
	1487	[N IV]	162.00	0.098	0.041	275.40
	1550	C IV	61.75	0.098	0.041	102.20
	1640-1663	He II ,O III	257.30	0.098	0.041	413.50
	1750	N III]	88.24	0.098	0.041	138.00
	1909	C III]	50.10	0.098	0.041	78.34

<sup>a</sup>In terms of  $H\beta=100$ , where optical fluxes are from Stanghellini et al. (2003), Shaw (2006).

<sup>b</sup>P-Cygni absorbed component was also detected corresponding to this feature. The flux corresponds to the redshifted emission line.

<sup>c</sup>Flux uncertainty  $\sim 25\%$

<sup>d</sup>Flux unceratinty  $\sim 15\%$

Table 3. Plasma Diagnostics

Name	$T_e^a$ [K]	$T_e^b$ [K]	$N_e^b$ [ $\text{cm}^{-3}$ ]	ref	EC
SMP 6	15600	14400	11400	LD06	4
SMP 8	...	$13700^{+1110}_{-1170}$	2770	SEA	2-3
SMP 13	...	$12800^{+1080}_{-940}$	2900	SEA	4
SMP 15	16200	12000	5000:	LD06	2-4
SMP 16	...	11800	5000:	LD06	0
SMP 18	...	$11860^{+800}_{-870}$	3590	SEA	0.5
SMP 20	...	$13820^{+1380}_{-1010}$	3880	SEA	1-2
SMP 24	...	$11620^{+910}_{-740}$	2780	SEA	1-2
SMP 25	...	21100	9800	LD06	6-7
SMP 26	...	18000	300	LD06	8
SMP 28	...	19200	20700	LD06	8

<sup>a</sup>Temperature for low excitation ions

<sup>b</sup>Adopted by Authors in reference

Table 4. Carbon Abundances

Name	$C^+/H^+$	$C^{2+}/H^+$	$C^{3+}/H^+$	ICF(C)	A(C)
SMP 6	$1.016 \times 10^{-5}$	$1.917 \times 10^{-4}$	$2.184 \times 10^{-5}$	1.0	$8.35^{+0.03}_{-0.03}$
SMP 8	...	$9.596 \times 10^{-5}$	$3.631 \times 10^{-5}$	1.0	$8.12^{+0.17}_{-0.13}$
SMP 13	$2.877 \times 10^{-5}$	$4.753 \times 10^{-4}$	$3.445 \times 10^{-5}$	1.0	$8.73^{+0.05}_{-0.15}$
SMP 15	$\geq 4.889 \times 10^{-6}$	$1.621 \times 10^{-4}$	$1.379 \times 10^{-5}$	1.0	$8.26^{+0.06}_{-0.07}$
SMP 16	$7.357 \times 10^{-5}$	$7.761 \times 10^{-5}$	$4.403 \times 10^{-6}$	1.0	$8.19^{+0.08}_{-0.1}$
SMP 18	$\geq 6.422 \times 10^{-5}$	$1.377 \times 10^{-4}$	$7.047 \times 10^{-7}$	1.0	$8.31^{+0.05}_{-0.20}$
SMP 20	$2.694 \times 10^{-5}$	$1.492 \times 10^{-4}$	$1.283 \times 10^{-6}$	1.0	$8.25^{+0.2}_{-0.22}$
SMP 24	...	$1.485 \times 10^{-4}$	...	1.02	$8.18^{+0.05}_{-0.25}$
SMP 25	...	$1.626 \times 10^{-6}$	$1.602 \times 10^{-6}$	1.38	$6.64^{+0.09}_{-0.13}$
SMP 26	...	$1.349 \times 10^{-4}$	$6.497 \times 10^{-5}$	1.45	$8.46^{+0.04}_{-0.05}$
SMP 28	...	$4.255 \times 10^{-6}$	$2.525 \times 10^{-6}$	1.34	$6.96^{+0.02}_{-0.03}$